Magnetocrystalline anisotropy in the Kondo-lattice compound CeAgAs₂

Rajib Mondal,[*] Rudheer Bapat, S. K. Dhar, and A. Thamizhavel[*]

Department of Condensed Matter Physics and Materials Science, Tata Institute of Fundamental Research,
Homi Bhabha Road, Colaba, Mumbai 400 005, India

We report on the single-crystal growth and anisotropic physical properties of CeAgAs₂. The compound crystallizes as an ordered variant of the HfCuSi₂-type crystal structure and adopts the orthorhombic space group *Pmca* (No. 57) with two symmetry-inequivalent cerium atomic positions in the unit cell. The orthorhombic crystal structure of the single crystal was confirmed from the powder x-ray diffraction and from electron diffraction patterns obtained from the transmission electron microscope. The anisotropic physical properties have been investigated on a good-quality single crystal by measuring the magnetic susceptibility, isothermal magnetization, electrical transport, and heat capacity. The magnetic susceptibility and magnetization measurements revealed that this compound orders antiferromagnetically with two closely spaced magnetic transitions at $T_{N1} = 6$ K and $T_{N2} = 4.9$ K. Magnetization studies have revealed a large magnetocrystalline anisotropy due to the crystalline electric field with an easy axis of magnetization along the [010] direction. The magnetic susceptibility measured along the [001] direction exhibited a broad hump in the temperature range 50 to 250 K, while typical Curie-Weiss behavior was observed along the other two orthogonal directions. The electrical resistivity and the heat capacity measurements revealed that CeAgAs₂ is a Kondo-lattice system with a magnetic ground state.

I. INTRODUCTION

One of the most widely investigated topics of research in condensed-matter physics during the last few decades has been the competition between the Ruderman, Kittel, Kasuya, and Yosida (RKKY) interaction and the Kondo effect in Ce- and Yb-based intermetallic compounds. The investigations of these compounds have discovered a plethora of new phenomena like heavy fermions [1,2], valence fluctuation [3], unconventional superconductivity [4,5], quantum phase transitions [6], etc. In recent years, many reports on Ce-based compounds have indicated they can be tuned to a quantum critical point with pressure as the tuning parameter [7–9]. All these interesting physical properties are due to the result of the hybridization of the localized $4f$ electron with the conduction electrons. A weak hybridization usually results in a magnetic ground state, while a stronger hybridization results in a weaker localization of the $4f$ electron pushing the system eventually to a nonmagnetic intermediate valence state. The hybridization strength and the effects due to the crystal electric field (CEF) depend on the atomic environment around the Ce atom in the unit cell, which includes the interatomic distances between the Ce and other atoms on different crystallographic sites. Most of the cerium-based compounds possess a single unique atomic position for the Ce atom in the unit cell. However, there are some cerium compounds which host multiple sites for Ce atoms in the unit cell [10], for example, Ce₇Ni₃ [11], Ce₂PdGe₃ [12], Ce₄Co₂Sn₅ [13], CeRuSn₃ [14], CeRhSn₃ [15], Ce₂Rh₃Ge [16], Ce₂RuZn₄ [17], etc. The compounds with multiple Ce

sites have been studied mostly in the polycrystalline form. But there have been some sporadic reports on single-crystalline Ce compounds possessing two or more Ce sites, for example, CeRuSn [18], Ce₃Al₁₁ [19], Ce₂Bi(Sb) [20], Ce₃Pd₂₀Si₆ [21], and, more recently, Ce₃PdIn₁₁ [22] and Ce₃PtIn₁₁ [23].

The interest in multiple-Ce-site compounds stems from the fact that different crystallographic environments surrounding the Ce atoms may result in different hybridization strengths and the resultant degree of localization. This, together with the RKKY exchange interaction, which may have different magnitudes at the multiple Ce sites, may give rise to interesting magnetic properties. The title compound, CeAgAs₂, crystallizing in the orthorhombic crystal structure also possesses two symmetry-inequivalent sites for Ce atoms. In CeAgAs₂ the two symmetry-inequivalent Ce sites have the same $4d$ Wyckoff position but with slightly different y and z values. In order to investigate anisotropic magnetic properties, we have grown and measured the physical properties of single-crystalline CeAgAs₂.

Compounds of the form CeTX_2, where T is a transition metal and X is either Sb or As, crystallize mostly in the HfCuSi₂-type crystal structure with the space group $P4/nmm$ (No. 129), which hosts a unique atomic position for the Ce atom at the $2c$ site. The anisotropic physical properties of CeTSb₂ have been studied quite extensively [24–26]. For example, CeAgSb₂ is a ferromagnet with the easy axis of magnetization along the [001] direction and a saturation moment of only $0.45\mu_B$/Ce, which remains constant up to fields as high as 45 T. On the other hand, the isostructural CeAuSb₂ becomes an antiferromagnet at 6 K and exhibits field-induced quantum criticality [27]. In view of the wide variety of magnetic properties exhibited by the antimonides, the arsenides of this series of compounds have also been

---

[*]Corresponding authors: mondal.rajib1988@gmail.com; thamizh@tifr.res.in

115160-1

synthesized and studied for their crystal structure and magnetism. The compounds of $CeTAs_2$ have been synthesized mostly in polycrystalline form [28–31]. In the present work, we were successful in growing the single crystals of $CeAgAs_2$ using the self-flux method and report the interesting anisotropic magnetic properties exhibited by this compound.

II. EXPERIMENT

We have employed high-temperature solution growth, or the so-called flux growth method, to grow single crystals of $CeAgAs_2$. Typically, for flux growth one of the constituents that has the lowest melting point is used as a flux (solvent) to grow the single crystal. But in $CeAgAs_2$ none of the elements possess a low melting point, and hence, we used the eutectic composition of Ag-As as a self-flux to grow the single crystals [32]. The binary phase diagram of Ag-As reveals a eutectic composition at 75:25 at. % of Ag:As, with a relatively low melting point of 540 °C. The starting materials of high-purity Ce (99.9% Ames Lab), Ag (99.99%), and As (99.999%) were taken in the ratio 1:37:14, which took into account the eutectic composition of the excess Ag:As flux. The elements were placed in a high-quality recrystallized alumina crucible and subsequently sealed in a quartz ampoule under partial pressure of argon gas. The ampoule was loaded in a resistive-heating box-type furnace and the temperature of the furnace was raised at a rate of 15 °C/h to 1050 °C and held there for about 24 h for homogenization of the solution. Then the furnace was cooled to 700 °C at a rate of 2 °C/h, at which point the contents of the ampoule were centrifuged to remove the flux. Large, shiny, flat plateletlike single crystals with a typical size of $10 \times 6 \times 0.3$ mm^3 were obtained. A similar procedure was employed to grow the nonmagnetic analog $LaAgAs_2$. The flat plane of the crystal corresponds to the (001) plane. Powder x-ray, Laue diffraction, and transmission electron microscopy (TEM) were performed on a few grown crystals to determine the phase purity, the crystallographic orientation, and the superstructure nature of the crystal. A crystal selected at random was cut into a bar-shaped sample using the spark erosion cutting machine for the anisotropic physical property measurements. The electrical resistivity, heat capacity, and magnetization measurements were performed in a physical property measurement system and magnetic property measurement system from Quantum Design.

III. EXPERIMENTAL RESULTS

A. X-ray diffraction

Since the crystals were grown completely from an off-stoichiometric melt, first, we performed a powder x-ray diffraction to confirm the phase purity. Figure 1(a) shows the powder x-ray diffraction pattern of our sample. It is evident from Fig. 1(a) that all the peaks can be indexed to the orthorhombic crystal structure of $CeAgAs_2$. At 38° for 2θ the peak marked by an asterisk is due to the impurity of the Ag:As flux. Here it may be pertinent to first recall that a detailed crystal structure analysis of $CeAgAs_2$ was previously performed by Demchyna *et al.* [28] which showed that unlike the other members of the CeTX_2 (T is a transition metal; X = Sb or As), $CeAgAs_2$ does not adopt the tetragonal HfCuSi$_2$-type
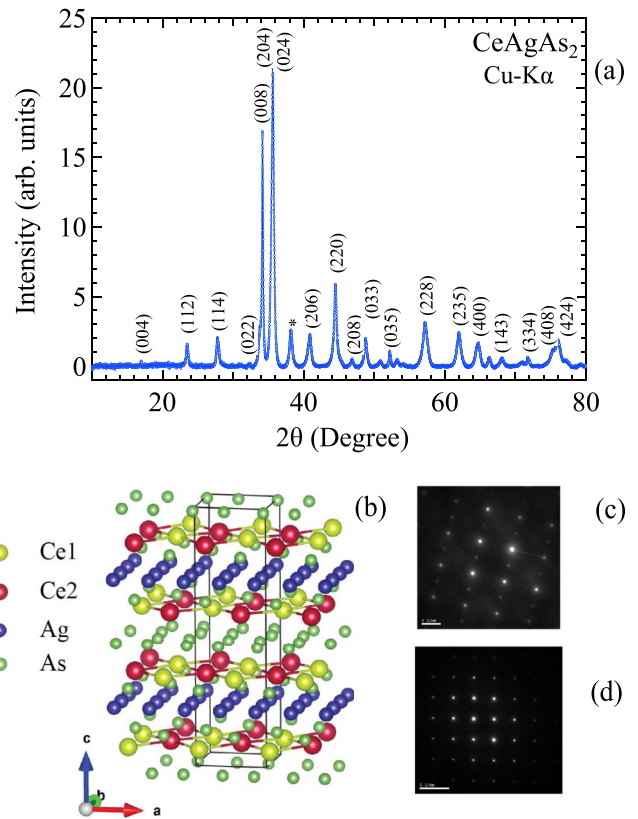

FIG. 1. (a) Powder x-ray diffraction pattern of $CeAgAs_2$, where the asterisk indicates the impurity peak due to Ag:As flux, (b) the crystal structure of $CeAgAs_2$, (c) TEM diffraction pattern depicting the superstructure spots in the orthorhombic $CeAgAs_2$, and (d) TEM diffraction pattern of the tetragonal $CeCuAs_2$, where the superstructure spots are absent.

crystal structure. It crystallizes in the orthorhombic crystal structure with the space group *Pmca* (No. 57) with lattice parameters $a = 5.7441$ Å, $b = 5.7696$ Å, and $c = 21.0074$ Å, which are related to the tetragonal HfCuSi$_2$ structure by $\sqrt{2}a_T$ and $2c_T$. The *Pmca* space group has two atomic positions for Ce atoms, Ce1 and Ce2 at $4d$ positions. The crystal structure of $CeAgAs_2$ is shown in Fig. 1(b). The nearest distance between the Ce1-Ce1 and Ce2-Ce2 atoms is 5.758 Å, while that of Ce1-Ce2 is 4.078 Å. From the Laue diffraction pattern we confirmed the flat plane of the crystal corresponds to the (001) plane. Well-defined spots with a clear symmetry pattern confirm the good quality of the grown single crystal. Furthermore, the superstructure nature of the unit cell along the c axis was observed using the transmission electron microscope, and the observed diffraction pattern is shown in Fig. 1(c). The diffused spots confirm the superstructure nature of the unit cell, while this is not observed in the TEM diffraction pattern of tetragonal $CeCuAs_2$, as shown in Fig. 1(d).

B. Magnetic susceptibility and magnetization

The temperature dependence of the dc magnetic susceptibility measured along the three principal crystallographic directions from 1.8 to 300 K is shown on a semilogarithmic scale in the main panel of Fig. 2(a). The magnetic
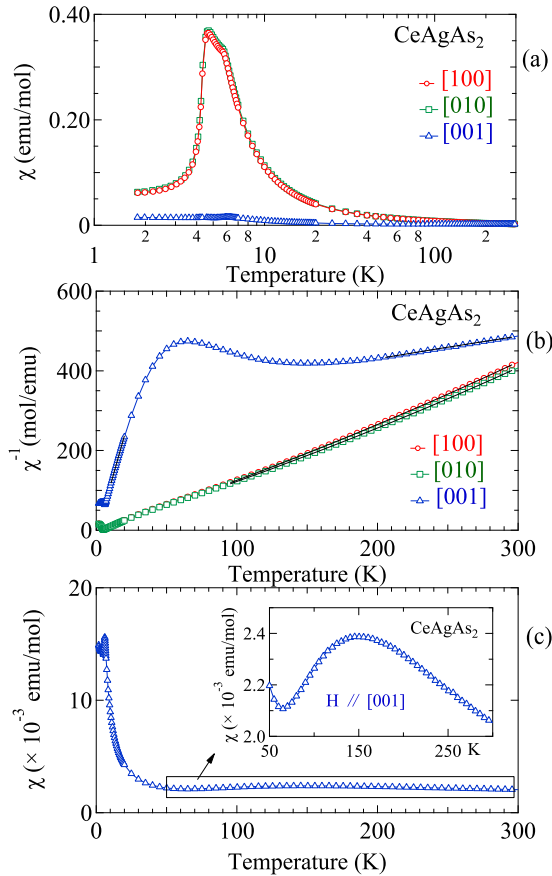
FIG. 2. (a) Temperature dependence of anisotropic magnetic susceptibility along the three principal crystallographic directions measured in a field of 5 kOe. The two magnetic transitions are clearly visible at 6 and 4.9 K, respectively. A huge drop in the magnetic susceptibility along the [100] and [010] directions is observed. (b) Inverse magnetic susceptibility and the modified Curie-Weiss fit for $T > 100$ K along $H \parallel (ab)$ plane and for $T > 200$ K for $H \parallel$ [001]. The Curie-Weiss fit was performed in the low-temperature region from 10 to 20 K for $H \parallel$ [001]. (c) Magnetic susceptibility along the [001] direction with a zoomed-in view in the temperature range from 50 to 300 K.

susceptibility along the [100] and [010] directions increases more rapidly below about 50 K and then exhibits a small cusp at 6 K followed by a sharp drop at 4.9 K, indicating two magnetic transitions. From the magnetization measurements (see below) and from previous neutron diffraction studies [31] on a polycrystalline sample, the two magnetic transitions are confirmed to be antiferromagnetic in nature. Just below the first antiferromagnetic transition at $T_{N1} = 6$ K, the magnetic susceptibility increases, and then it drops down rapidly below $T_{N2} = 4.9$ K. The drop in the magnetic susceptibility ascertains the antiferromagnetic nature of the transition at 4.9 K and confirms the easy axis of magnetization as [100] or [010]. For $H \parallel$ [001], at T_{N1} the susceptibility shows a drop followed by a small rise at the second transition at T_{N2}, which is virtually temperature independent at lower temperatures, suggesting [001] as the hard axis of magnetization. The anisotropy within the ab plane is weak, while the anisotropy between the ab plane and the c axis is quite large. The curvilinear behavior

of the inverse magnetic susceptibility along the [100] and [010] directions indicates the simple Curie-Weiss law cannot be used to analyze the magnetic susceptibility data. Hence, we have employed the modified Curie-Weiss law, $\chi^{-1} = (\chi_0 + \frac{C}{(T - \theta_p)})^{-1}$, to fit the inverse magnetic susceptibility above 100 K for the [100] and [010] directions. Here χ_0 is the temperature independent term constituting the diamagnetic susceptibility due to the core electrons and the Pauli spin susceptibility of the conduction electrons, and C is the Curie constant. We have obtained $\chi_0 = -4.434 \times 10^{-4}$ emu/mol, an effective magnetic moment of $2.59\mu_B$/Ce, and the paramagnetic Weiss temperature $\theta_p = -0.20$ K for $H \parallel$ [100] and $\chi_0 = -4.797 \times 10^{-4}$ emu/mol, $\mu_{eff} = 2.66\mu_B$/Ce, and $\theta_p = -2.32$ K for the $H \parallel$ [010] direction. The obtained effective magnetic moment values are very close to the theoretical value of trivalent Ce, suggesting a local moment behavior. The modified Curie-Weiss law could not result in a good fitting for the $H \parallel$ [001] direction. However, if we fix the effective magnetic moment to $2.54\mu_B$/Ce, a reasonably good fitting is obtained in the temperature range from 250 to 300 K with $\chi_0 = 7.079 \times 10^{-4}$ emu/mol and $\theta_p = -299$ K, as shown in Fig. 2(b). Also shown in Fig. 2(b) is the low-temperature Curie-Weiss fit in the range 10 K $< T <$ 20 K for the $H \parallel$ [001] direction. The fit resulted in a value of $\mu_{eff} = 0.808\mu_B$/Ce and $\theta_p = 0.75$ K. The obtained value of μ_{eff} is close to the $J = 1/2$ doublet ground-state value, and θ_p is also close to zero, indicating a weak exchange interaction in the doublet ground state. Figure 2(c) shows the magnetic susceptibility for the $H \parallel$ [001] direction, which is very weak (of the order of 10^{-3} emu/mol). It is obvious from the susceptibility data that the Curie-Weiss behavior is absent, and a broad hump is observed in the temperature range from 50 to 300 K. This type of behavior is usually attributed to mixed-valent or intermediate-valent character [16,33]. However, in the present case, we shall see that it arises due to a strong crystal field effect.

The isothermal magnetization measured at $T = 2$ K is shown in Fig. 3(a). In agreement with the magnetic susceptibility data presented above, the isothermal magnetization exhibits an easy-plane magnetocrystalline anisotropy. A very sharp spin-flip-like metamagnetic transition is observed at a field of 7.5 kOe for the $H \parallel$ [100] and [010] directions, and for fields greater than 10 kOe, the magnetization almost saturates. The saturation value of the magnetization is about $1.2\mu_B$/Ce, which is much less than that expected for the free-ion value of Ce in its trivalent state ($g_J J = 2.14\mu_B$/Ce). On the other hand, the magnetization along [001] increases very gradually and attains a value of only $0.18\mu_B$ at 70 kOe, thus confirming it as the hard axis of magnetization. The low saturation value of the magnetic moment for fields as high as 70 kOe suggests strong evidence of a CEF and/or a Kondo effect. We have also determined the temperature dependence of isothermal magnetization for $H \parallel$ [100], and it is shown in Fig. 3(b). We found that the critical field at which the metamagnetic transition appears shifts to lower fields and broadens as the temperature is increased, and finally, for temperatures larger than T_{N1} the magnetization shows an almost linear dependence on field in the paramagnetic state, as expected in antiferromagnetic compounds. From the differential plots of the isothermal magnetization measured at different
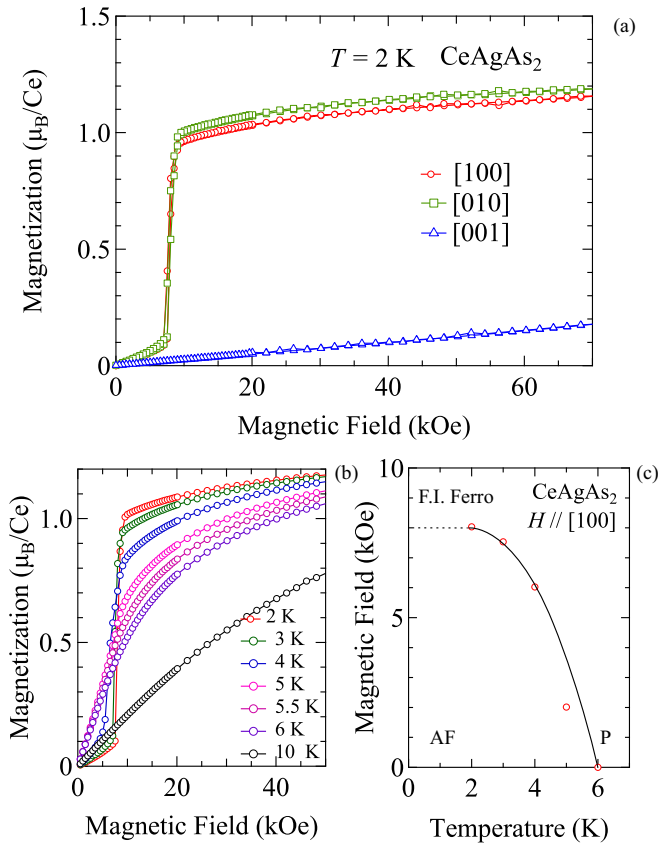
FIG. 3. Isothermal magnetization measured at $T = 2$ K along the three principal crystallographic directions. A sharp first-order-like metamagnetic transition is observed at 7.5 kOe for the $H \parallel [100]$ and [010] directions. (b) Isothermal magnetization plots measured at various temperatures for the $H \parallel [100]$ direction and (c) magnetic phase diagram derived from the isothermal magnetization plots. Here P refers to the paramagnetic state, AF refers to the antiferromagnetic state, and F.I. Ferro refers to the field-induced ferromagnetic state. The solid and dotted lines are guides to the eyes.

temperatures, we have constructed a magnetic phase diagram, as shown in Fig. 3(c). At low temperatures and for fields less than 8 kOe, CeAgAs$_2$ is in a purely antiferromagnetic state, and it enters into the field-induced ferromagnetic state at higher fields.

C. Electrical resistivity

The temperature dependence of the electrical resistivity of CeAgAs$_2$ for current parallel to the [100] direction or (ab) plane is shown in the main panel of Fig. 4. We could not measure the resistivity for $J \parallel [001]$ because of the small thickness of the sample. At room temperature the electrical resistivity has a value of about 700 $\mu\Omega$ cm, which is quite large. As the temperature decreases, the resistivity decreases gradually and exhibits a very broad maximum centered around 100 K, which may be attributed to the thermal depopulation of the CEF levels. Below 100 K, the resistivity falls off more rapidly, showing a broad minimum around 25 K and then increases gradually. The resistivity data in zero field show a linear logarithmic temperature dependence in the range of 20 to 6 K, suggesting that CeAgAs$_2$ is a Kondo-lattice system
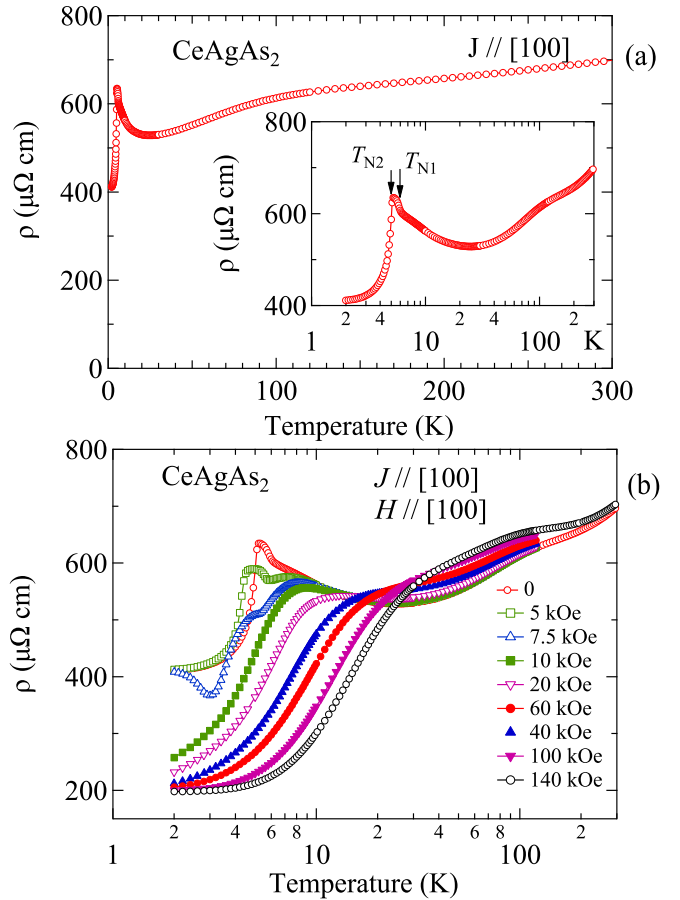

FIG. 4. (a) Temperature dependence of electrical resistivity in the temperature range from 1.8 to 300 K. The inset shows the resistivity plot in the semilog scale, where the two magnetic transitions are clearly seen. (b) Magnetic field dependence of electrical resistivity for the $J \parallel [100]$ and $H \parallel [100]$ directions.

[see the inset of Fig. 4(a)]. At 6 K a sudden change in slope is observed, and the electrical resistivity increases more rapidly, which marks T_{N1}. At $T_{N2} = 4.9$ K, the electrical resistivity drops due to the reduction in the spin disorder scattering, thus confirming the two magnetic transitions observed from the magnetic susceptibility data. The increase in the electrical resistivity just below T_{N1} is typical of compounds that exhibit a superzone gap [34], which occurs due to the difference in the lattice periodicity and magnetic periodicity. But here in the present case, the presence of superzone gap is ruled out because the previous neutron diffraction studies have revealed the propagation vector $k = [0, 0, 0]$ [31]. Hence, the increase in the electrical resistivity in the region $T_{N2} < T < T_{N1}$ is mainly attributed to the spin fluctuation effect presumably due to the isosceles triangular arrangements of the Ce1 and Ce2 atoms along the [100] direction. It should be noted that the electrical resistivity begins to drop at T_{N2} from a value of 634 to about 411 $\mu\Omega$ cm at 2 K, the lowest temperature measured. The huge value of the residual resistivity is attributed to the spin fluctuations and some crystallographic disorder. The nearly linear logarithmic upturn in the resistivity below 25 K is reminiscent of a Kondo-lattice system.
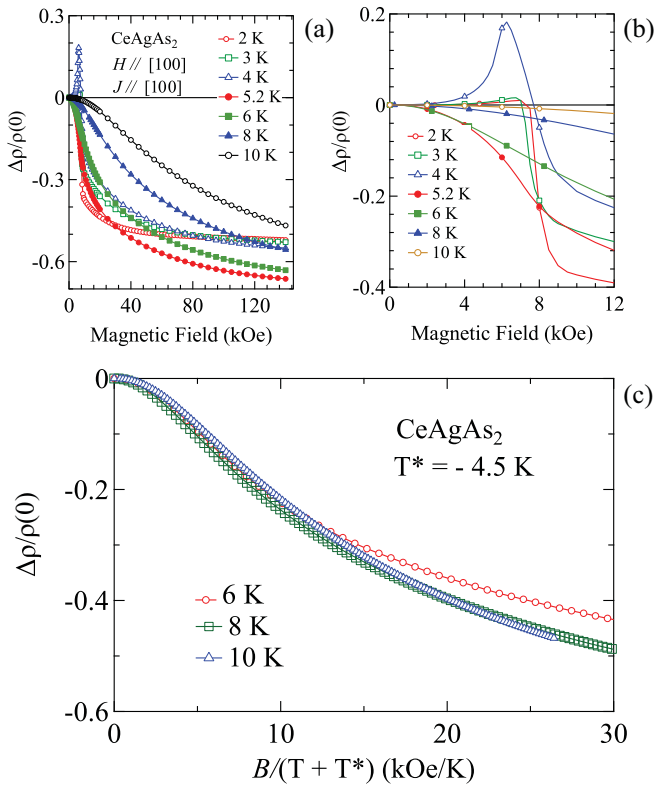
FIG. 5. (a) Isothermal magnetoresistance MR = $\frac{\Delta\rho}{\rho(0)} = \frac{\rho(B)-\rho(0)}{\rho(0)}$ for $CeAgAs_2$ as a function of applied magnetic field for $J \parallel [100]$ and $H \parallel [100]$. (b) The low-field part of the isothermal magnetoresistance with sparse markers for clarity and (c) normalized magnetoresistance in the paramagnetic region plotted as a function of $B/(T+T^*)$.

We have also measured the electrical resistivity under applied magnetic fields, and the plots are shown in Fig. 4(b). The magnetic field is applied along the easy axis of the magnetization direction. With the increase in the magnetic field, the two magnetic transition temperatures decrease and are not discernible for fields greater than 10 kOe down to 2 K. This type of behavior is generally observed in antiferromagnetic systems. In an applied field of 7.5 kOe, the electrical resistivity shows an upturn at 3 K, and the increasing trend is seen down to 2 K. This anomalous behavior of the electrical resistivity may be attributed to the spin-flip-like metamagnetic transition observed in the isothermal magnetization at 7.5 kOe; it is observed only at this field and not at higher or lower magnetic fields. It is interesting to note that the residual resistivity decreases substantially with increasing magnetic fields, suggesting a significant magnetic contribution due to spin fluctuations which are suppressed by applied magnetic fields.

The isothermal field-dependent magnetoresistance is shown in Fig. 5(a), and the low-field part as a zoomed-in view, with sparse markers, is shown in Fig. 5(b). The variation of magnetoresistance with field is in good agreement with the magnetization data presented earlier. At the lowest temperature of 2 K, the magnetoresistance is slightly positive, and a sudden change in magnitude is observed in the negative direction at 7.5 kOe, suggesting the field-induced

ferromagnetic state. A similar behavior is observed for 3 K data as well. At $T = 4$ K, the magnetoresistance exhibits a sharp peak at 6.3 kOe and becomes negative at 7.5 kOe. This may be attributed to the effect of field on spin fluctuations at this temperature. In the paramagnetic region, the normalized magnetoresistance can be mapped onto a single curve if plotted as a function of $B/(T + T^*)$, where T^* is the characteristic temperature, often identified as the Kondo temperature [35]. Our experimental data taken at selected temperatures can be mapped onto a single curve with a characteristic temperature T^* of about -4.5 K. A negative T^* value was obtained for several antiferromagnetic Kondo-lattice compounds [36,37], and it was attributed to the ferromagnetic correlations. From the magnetic measurements it is clear that $CeAgAs_2$ orders antiferromagnetically. The ferromagnetic correlations in this compound arise due to the parallel alignment of magnetic moments in the layers of the ab plane which are antiparallel along the c axis as inferred from the neutron diffraction studies by Doert et $al.$ [31].

D. Specific heat

The temperature dependence of the heat capacity of $CeAgAs_2$ and the nonmagnetic reference $LaAgAs_2$ in the temperature range 2–200 K is shown in the main panel of Fig. 6(a). The heat capacity of $CeAgAs_2$ is larger than that of $LaAgAs_2$ at all temperatures. The bulk nature of the magnetic transitions observed in magnetization and resistivity is confirmed by the two sharp peaks at $T_{N1} = 6$ K and $T_{N2} = 4.9$ K with appreciable magnitude [bottom inset of Fig. 6(a)]. The low-temperature data of $LaAgAs_2$ in the temperature range (2 to ~ 6 K) was fitted to the expression $C = \gamma T + \beta T^3$, where the Sommerfeld coefficient γ is the electronic contribution and β is the phonon contribution to the heat capacity. The γ and β values thus obtained are 1.20 mJ/K^2 mol and 0.413 mJ/K^4 mol, respectively. The top inset in Fig. 6(a) shows the low-temperature part of the heat capacity of $CeAgAs_2$ in the form of C/T versus T^2. Similarly, we have obtained the γ and β values for $CeAgAs_2$ as 61.3 mJ/K^2 mol and 76.12 mJ/K^4 mol, respectively. There is a substantial increase in γ due to the Kondo effect. The enhanced value of β is attributed to spin waves in $CeAgAs_2$, which follow a T^3 dependence in antiferromagnets. We have estimated the magnetic part of the heat capacity using the usual method of subtracting the heat capacity of $LaAgAs_2$ from that of $CeAgAs_2$. The obtained C_{4f} contribution to the heat capacity is shown in Fig. 6(b). The peak around 100 K is the Schottky peak arising from the thermal variation of the population of CEF levels. The magnetic entropy that is released at 6 K is only 70% of $R\ln 2$, while the remaining 30% of the entropy is released at around 30 K. This indicates that the ground state is a doublet. The reduction in the magnetic entropy is mainly attributed to the Kondo effect. Similarly, the jump in the magnetic part (ΔC_{mag}) of the heat capacity amounts to 9.02 J/K mol at T_{N1} and 4.53 J/K mol at T_{N2}. The reduced jump in the heat capacity, compared to the value expected for the $S = 1/2$ (12.5 J/K mol) doublet state, supports the existence of the Kondo effect in $CeAgAs_2$.

We have also measured the field dependence of the heat capacity of $CeAgAs_2$. When the field was applied parallel to
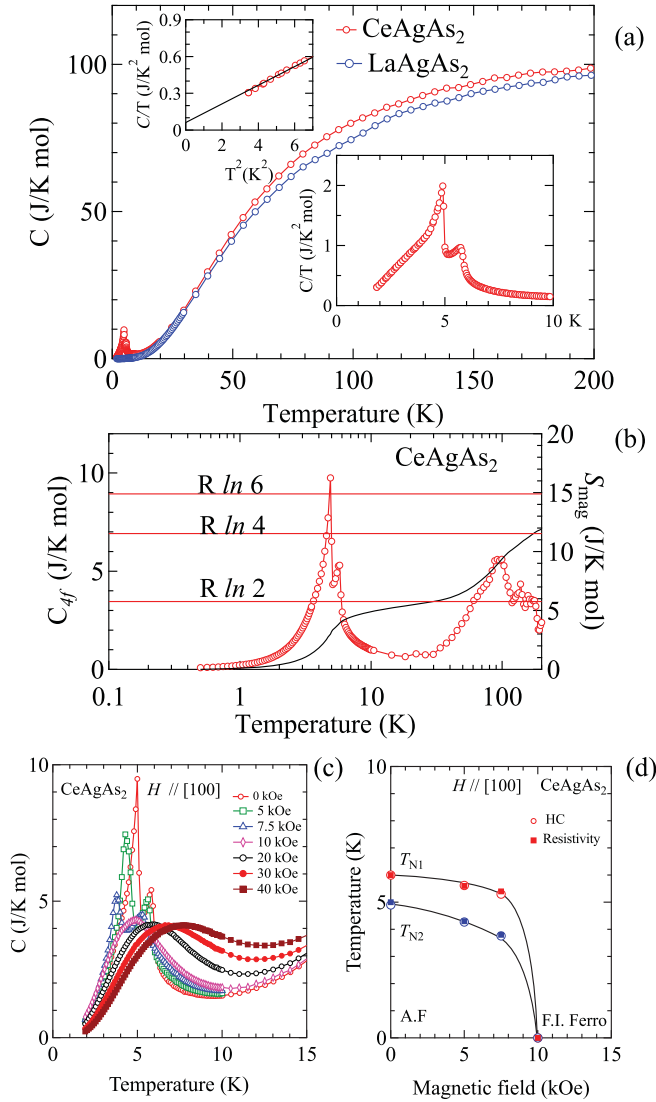
FIG. 6. (a) Temperature dependence of heat capacity of CeAgAs$_2$ and the nonmagnetic LaAgAs$_2$. The top inset shows the low-temperature part of C/T versus T^2 and the bottom inset shows the low-temperature part of specific heat in the form of C/T versus T of CeAgAs$_2$. (b) The $4f$-derived part of the heat capacity along with the entropy. (c) Field dependence of the heat capacity. (d) Variation of T_{N1} and T_{N2} with magnetic field. For fields above 10 kOe, at low temperature, the system enters into a field-induced ferromagnetic state, while for fields less than 10 kOe it is in an antiferromagnetic state. The solid lines are guide to the eyes.

the flat plane of the crystal, there was no change in the heat capacity (not shown here for brevity). Hence, the crystals were aligned in such a way that the applied magnetic field is parallel to the easy axis of magnetization, viz., [100]. Figure 6(c) shows the magnetic field dependence of the heat capacity at various applied magnetic fields. It is evident that as the applied magnetic field is increased, the Néel temperatures shift towards lower temperature. At a field of 7.5 kOe, where the metamagnetic jump is observed in the magnetization data, there is a sudden change in the magnitude of the heat capacity, and for fields greater than 7.5 kOe, the heat capacity shows only a broad hump which shifts towards the right side at

higher fields. At the lowest temperature measured, the in-field heat capacity is lower than its zero-field value, which can be attributed to the breakdown of Kondo coupling, between the localized $4f$ and conduction electrons with applied field [38]. The variation of T_{N1} and T_{N2} with magnetic field is shown in Fig. 6(d). Both transitions decrease towards low temperature until 7.5 kOe, beyond which the magnetic transitions are not discernible. At low temperatures and for fields greater than 10 kOe, the system enters the field-induced ferromagnetic state. The solid lines in Fig. 6(d) are a guide to the eyes.

IV. DISCUSSION

The magnetic measurements along the three principal crystallographic directions revealed a strong anisotropy between the ab plane and the c axis. Furthermore, there is a strong suppression of the ordered moment and a reduced heat capacity jump together with a Schottky-like peak in the C_{4f} heat capacity caused by the CEF effect. Hence, we analyzed the magnetocrystalline anisotropy based on the point charge model. For the purpose of the CEF analysis, we have plotted the magnetic susceptibility in the form of $1/(\chi - \chi_0)$, where χ_0 was determined from the modified Curie-Weiss fit, as mentioned earlier. There are two Ce sites occupying the same $4d$ Wyckoff position, with the same x coordinate, while y and z are different [28]. Assuming that the $4d$ site which hosts both Ce atoms has an identical crystallographic environment, we performed the CEF analysis. The point symmetry of the $4d$ Wycoff position is m and hence possesses monoclinic site symmetry. For monoclinic site symmetry, the $2J + 1$ ground state of the Ce atom splits into three doublets. In order to reduce the number of fitting parameters in the CEF analysis, we used the CEF Hamiltonian for the orthorhombic site symmetry, which is given by

$$\mathcal{H}_{\text{CEF}} = B_2^0 O_2^0 + B_2^2 O_2^2 + B_4^0 O_4^0 + B_4^2 O_2^2 + B_4^4 O_4^4, \quad (1)$$

where B_n^m are the CEF parameters and O_n^m are the Stevens operators [39,40]. In the above CEF Hamiltonian we have ignored the sixth-order terms as they are zero for the Ce atom. The magnetic susceptibility including the molecular field contribution λ is given by

$$\chi^{-1} = \chi_{\text{CEF}}^{-1} - \lambda_i, \quad (2)$$

where χ_{CEF} is the CEF susceptibility. The expression for the CEF susceptibility is given in our previous report [38]. We have also analyzed the isothermal magnetization by using the following expression:

$$M_i = g_j \mu_B \sum_n \langle n | J_i | n \rangle \frac{e^{-E_n/k_B T}}{\sum_n e^{-E_n/k_B T}}, \quad (3)$$

where E_n and the eigenfunction $|n\rangle$ are determined by diagonalizing the total Hamiltonian

$$\mathcal{H} = \mathcal{H}_{\text{CEF}} - g_J \mu_B J_i (H + \lambda_i M_i), \quad (4)$$

where $\mathcal{H}_{\text{CEF}}$ is given by Eq. (1), the second term is the Zeeman term, and the third is the molecular field term.

In Fig. 7(a) we show the calculated CEF curves as solid lines, which reproduce reasonably the observed experimental susceptibility along the two principal crystallographic directions, viz., the [100] and [001] directions. We do not show
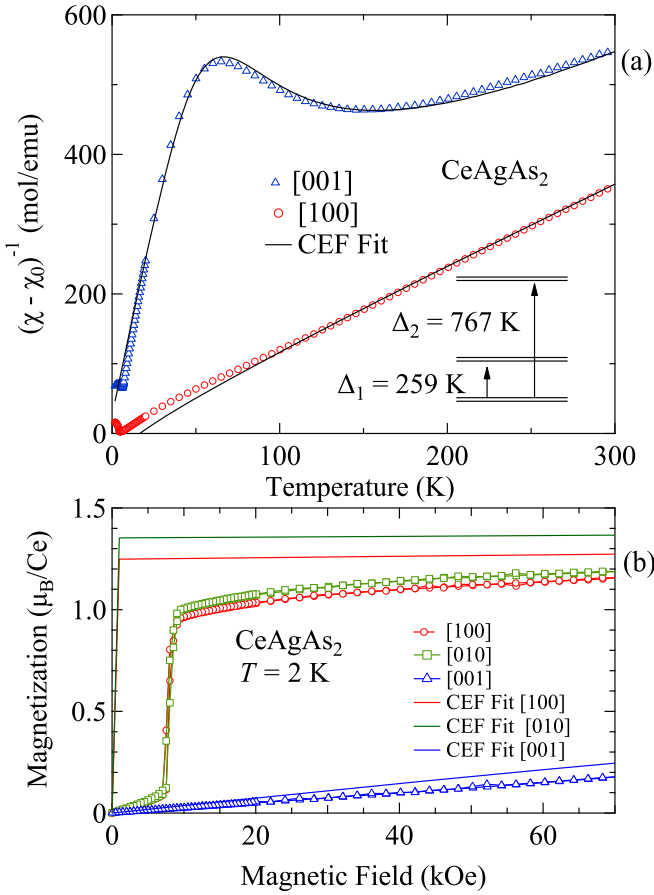
FIG. 7. (a) Temperature dependence of the inverse magnetic susceptibility plotted as $1/(\chi - \chi_0)$. The solid lines are fits to Eq. (2). (b) CEF fits to the isothermal magnetization curves of CeAgAs$_2$ at 2 K along the principal crystallographic directions.

the inverse susceptibility plot of the [010] direction as it overlaps with the [100] direction. The CEF analysis provides a good fit to the experimental data. It nicely reproduces the broad peak in the susceptibility along the [001] direction. The CEF parameters and the energy levels thus obtained from the diagonalization of the CEF Hamiltonian are given in Table I. The $2J + 1$ degenerate $J = 5/2$ level is split into

TABLE I. CEF fit parameters, energy levels, and wave functions.

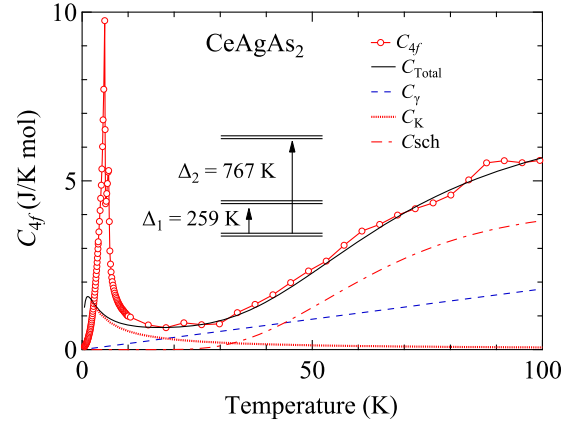| CEF parameters					
B_2^0 (K)	B_2^2 (K)	B_4^0 (K)	B_4^2 (K)	B_4^4 (K)	λ_i (emu/mol)$^{-1}$
5.79	−2.49	−2.40	−1.18	1.74	$\lambda_x = 30$, $\lambda_y = 30$, $\lambda_z = -25$
Energy level	Wave functions				
E (K)	$\vert+\tfrac{5}{2}\rangle$	$\vert+\tfrac{3}{2}\rangle$	$\vert+\tfrac{1}{2}\rangle$	$\vert-\tfrac{1}{2}\rangle$	$\vert-\tfrac{3}{2}\rangle$	$\vert-\tfrac{5}{2}\rangle$
767	0	0.996	0	0.014	0	0.0901
767	0.0901	0	0.014	0	0.996	0
259	0	−0.0865	0	−0.167	0	0.982
259	0.982	0	0.167	0	0.0865	0
0	0	−0.0288	0	0.986	0	0.165
0	0.165	0	0.986	0	−0.0288	0

FIG. 8. The $4f$ contribution of the heat capacity of CeAgAs$_2$. The thick solid line is the calculated C_{4f} based on Eq. (5).

three doublets at energies 0, 259, and 767 K. The ground state is predominantly $\vert\pm\tfrac{1}{2}\rangle$ with mixing from the $\vert\pm\tfrac{5}{2}\rangle$ and $\vert\pm\tfrac{3}{2}\rangle$ states. The molecular field constant is highly anisotropic, with positive values in the ab plane along the a and b axes, while it is negative along the c axis. This is consistent with the alignment of the magnetic moments, where the intralayer interactions in the ab plane are ferromagnetic, and the interlayer interaction along c axis is antiferromagnetic. Figure 7(b) shows the CEF analysis of the isothermal magnetization at 2 K. The small discrepancy between the calculated CEF curve and the experimental magnetization may be attributed to the fact that the CEF calculations do not take into account the Kondo effect. However, the anisotropy in the magnetization plots is clearly explained semiquantitatively by the present set of crystal field parameters.

The value of crystal field split energy levels of the $2J + 1$ ground state of the Ce- atom was used to analyze the heat capacity data. The $4f$ contribution of the heat capacity in the paramagnetic state can be expressed as the contribution of the electronic, Kondo, and the Schottky terms as

$$C_{4f} = C_{\text{el}} + C_{\text{K}} + C_{\text{Sch}}. \tag{5}$$

C_{el} is the electronic heat capacity defined by γT, while the expressions for C_{K} and C_{Sch} are given in Ref. [41]. The black solid line in Fig. 8 is the calculated curve based on Eq. (5). The energy levels obtained from the CEF analysis of the magnetic susceptibility data reproduce well the Schottky heat capacity. We obtain a Kondo temperature of 2.5 K. An estimation of the Kondo temperature in the mean-field model can also be obtained from the jump in C_{4f} of a Kondo system using the expression given by Blanco *et al.* [42]. The jump in the magnetic part of the heat capacity at T_{N2} amounts to 9.02 J/K mol, which results in a T_K/T_N value of 0.35 and hence a Kondo temperature of 1.72 K, which is close to the value obtained above using Eq. (5). It should be mentioned here that thermopower measurements would help us to ascertain the estimated value of T_K. Although our estimation of the crystal field levels from the magnetic susceptibility data explains the Schottky heat capacity well, which may be taken as a consistency check, for a precise determination of these levels, inelastic neutron diffraction has to be performed, which is planned as a future work. From our experimental

data and the calculations we find that the RKKY interaction in $CeAgAs_2$ prevails over the Kondo interaction, leading to a magnetically ordered ground state. Since external pressure enhances the Kondo temperature and $T_K \simeq T_N$ in $CeAgAs_2$, it would be interesting to study the effect of pressure on the magnetic behavior of this compound, in particular to probe whether pressure tunes $CeAgAs_2$ to a quantum critical point.

V. SUMMARY

We were successful in growing a single crystal of $CeAgAs_2$ and its nonmagnetic analog $LaAgAs_2$ with the flux method using a Ag:As eutectic composition as self-flux. From the x-ray diffraction and the TEM analysis we confirmed the superstructure in $CeAgAs_2$ single crystals, which results in an orthorhombic variant of the $HfCuSi_2$-type tetragonal crystal structure, with two distinct crystallographic sites for the Ce atom. The RKKY-type interaction results in two magnetic transitions at $T_{N1} = 6$ K and $T_{N2} = 4.9$ K. The magnetic susceptibility is highly anisotropic, and it exhibits a broad hump in the temperature range from 50 to 300 K for field parallel to the [001] direction. From the analysis of magnetization based on the point charge model of crystal electric field combined with the heat capacity data, it was confirmed that this broad hump is due to the crystal electric field and not due to the intermediate valence or mixed valence of Ce atoms. The anisotropy in the magnetic susceptibility can also be clearly explained by the crystal field analysis, with the two excited states at 259 and 767 K, respectively. The magnetic easy axis was found to be along the [100] or [010] direction, which is in agreement with previous neutron diffraction studies. The negative logarithmic increase in the electrical resistivity at low temperature in the paramagnetic region together with the reduced magnetic moment and reduced heat capacity jump at the magnetic transition confirms the presence of Kondo interaction in this compound.

[1] Z. Fisk, J. L. Sarrao, J. L. Smith, and J. D. Thompson, Proc. Natl. Acad. Sci. U.S.A. **92**, 6663 (1995).

[2] J. Flouquet, D. Aoki, F. Bourdarot, F. Hardy, E. Hassinger, G. Knebel, T. D. Matsuda, C. Meingast, C. Paulsen, and V. Taufour, J. Phys.: Conf. Ser. **273**, 012001 (2011).

[3] J. M. Lawrence, P. S. Riseborough, and R. D. Parks, Rep. Prog. Phys. **44**, 1 (1981).

[4] Y. Ōnuki, R. Settai, K. Sugiyama, T. Takeuchi, T. C. Kobayashi, and Y. Haga, J. Phys. Soc. Jpn. **73**, 769 (2004).

[5] R. Settai, T. Takeuchi, and Y. Onuki, J. Phys. Soc. Jpn. **76**, 051003 (2007).

[6] P. Gegenwart, Q. Si, and F. Steglich, Nat. Phys. **4**, 186 (2008).

[7] Z. F. Weng, M. Smidman, L. Jiao, X. Lu, and H. Q. Yuan, Rep. Prog. Phys. **79**, 094503 (2016).

[8] I. Sugitani, Y. Okuda, H. Shishido, T. Yamada, A. Thamizhavel, E. Yamamoto, T. D. Matsuda, Y. Haga, T. Takeuchi, R. Settai, and Y. Ōnuki, J. Phys. Soc. Jpn. **75**, 043703 (2006).

[9] Y. Ōnuki, R. Settai, Y. Miura, H. Tsutsumi, F. Honda, and H. Harima, Phys. Status Solidi B **250**, 583 (2013).

[10] K. A. Gshneidner, Jr. and V. K. Pecharsky, Phys. B (Amsterdam, Neth.) **223–224**, 131 (1996).

[11] K. Umeo, Y. Echizen, M. H. Jung, T. Takabatake, T. Sakakibara, T. Terashima, C. Terakura, C. Pfleiderer, M. Uhlarz, and H. v. Löhneysen, Phys. Rev. B **67**, 144408 (2003).

[12] R. E. Baumbach, A. Gallagher, T. Besara, J. Sun, T. Siegrist, D. J. Singh, J. D. Thompson, F. Ronning, and E. D. Bauer, Phys. Rev. B **91**, 035102 (2015).

[13] M. Pani, P. Manfrinetti, A. Palenzona, S. K. Dhar, and S. Singh, J. Alloys Compd. **299**, 39 (2000).

[14] V. K. Anand, D. T. Adroja, D. Britz, A. M. Strydom, J. W. Taylor, and W. Kockelmann, Phys. Rev. B **94**, 014440 (2016).

[15] V. K. Anand, D. T. Adroja, A. D. Hillier, W. Kockelmann, A. Fraile, and A. M. Strydom, J. Phys.: Condens. Matter **23**, 276001 (2011).

[16] M. Falkowski and A. M. Strydom, J. Phys.: Condens. Matter **27**, 395601 (2015).

[17] V. Eyert, E.-W. Scheidt, W. Scherer, W. Hermes, and R. Pöttgen, Phys. Rev. B **78**, 214420 (2008).

[18] J. Fikáček, J. Prokleška, J. Prchal, J. Custers, and V. Sechovský, J. Phys.: Condens. Matter **25**, 416006 (2013).

[19] C. S. Garde, T. Takeuchi, Y. Nakano, Y. Takeda, Y. Ota, Y. Miyauchi, K. Sugiyama, M. Hagiwara, K. Kindo, F. Honda, R. Settai, and Y. Ónuki, J. Phys. Soc. Jpn. **77**, 124704 (2008).

[20] A. Oyamada, A. Isobe, H. Kitazawa, A. Ochiai, T. Suzuki, and T. Kasuya, J. Phys. Soc. Jpn. **62**, 1750 (1993).

[21] A. Prokofiev, J. Custers, M. Kriegisch, S. Laumann, M. Müller, H. Sassik, R. Svagera, M. Waas, K. Neumaier, A. M. Strydom, and S. Paschen, Phys. Rev. B **80**, 235107 (2009).

[22] M. Kratochvílová, J. Prokleška, K. Uhlířová, V. Tkáč, M. Dušek, V. Sechovský, and J. Custers, Sci. Rep. **5**, 15904 (2015).

[23] J. Custers, M. Diviš, and M. Kratochvílová, J. Phys.: Conf. Ser. **683**, 012005 (2016).

[24] K. D. Myers, S. L. Bud'ko, I. R. Fisher, Z. Islam, H. Kleinke, A. H. Lacerda, and P. C. Canfield, J. Magn. Magn. Mater. **205**, 27 (1999).

[25] T. Takeuchi, A. Thamizhavel, T. Okubo, M. Yamada, N. Nakamura, T. Yamamoto, Y. Inada, K. Sugiyama, A. Galatanu, E. Yamamoto, K. Kindo, T. Ebihara, and Y. Ōnuki, Phys. Rev. B **67**, 064403 (2003).

[26] A. Thamizhavel, T. Takeuchi, T. Okubo, M. Yamada, R. Asai, S. Kirita, A. Galatanu, E. Yamamoto, T. Ebihara, Y. Inada, R. Settai, and Y. Ōnuki, Phys. Rev. B **68**, 054427 (2003).

[27] L. Balicas, S. Nakatsuji, H. Lee, P. Schlottmann, T. P. Murphy, and Z. Fisk, Phys. Rev. B **72**, 064422 (2005).

[28] R. Demchyna, J. P. F. Jemetio, Yu. Prots, Th. Doert, L. G. Akselrud, W. Schnelle, Yu. Kuz'ma, and Yu. Grin, Z. Anorg. Allg. Chem. **630**, 635 (2004).

[29] M. Szlawska and D. Kaczorowski, J. Alloys Compd. **451**, 464 (2008).

[30] M. Eschen and W. Jeitschko, Z. Naturforsch. B **58**, 399 (2003).

[31] Th. Doert, A. Schneidewind, M. H olzel, O. Stockert, D. Rutzinger, and M. Ruck, J. Magn. Magn. Mater. **324**, 1157 (2012).

[32] M. R. Baren, *Binary Alloy Phase Diagrams*, edited by T. B. Massalski (ASM International, Ohio, USA, 1990), Vol. 1, p. 10.

[33] D. T. Adroja, S. K. Malik, B. D. Padalia, and R. Vijayaraghavan, Phys. Rev. B **39**, 4831 (1989).

[34] P. Kumar Das, N. Kumar, R. Kulkarni, A. Thamizhavel, and S. K. Dhar, J. Phys.: Condens. Matter **24**, 146003 (2012).

[35] P. Schlottmann, Phys. Rep. **181**, 1 (1989).

[36] A. P. Pikul, D. Kaczorowski, T. Plackowski, A. Czopnik, H. Michor, E. Bauer, G. Hilscher, P. Rogl, and Yu. Grin, Phys. Rev. B **67**, 224417 (2003).

[37] A. P. Pikul, D. Kaczorowski, Z. Bukoski, T. Plackowski, and K. Gofryk, J. Phys.: Condens. Matter **16**, 6119 (2004).

[38] P. Kumar Das, N. Kumar, R. Kulkarni, and A. Thamizhavel, Phys. Rev. B **83**, 134416 (2011).

[39] K. W. H. Stevens, Proc. Phys. Soc. London, Sect. A **65**, 209 (1952).

[40] M. T. Hutchings, in *Solid State Physics: Advances in Research and Applications*, edited by F. Seitz and B. Turnbull (Academic Press Inc., New York, 1965), Vol. 16, p. 227.

[41] A. Maurya, R. Kulkarni, A. Thamizhavel, D. Paudyal, and S. Kumar Dhar, J. Phys. Soc. Jpn. **85**, 034720 (2016).

[42] J. A. Blanco, M. dePodesta, J. I. Espeso, J. C. Gómez Sal, C. Lester, K. A. McEwen, N. Patrikios, and J. Rodríguez Fernández, Phys. Rev. B **49**, 15126 (1994).